

# Influence of Refractive Index to Plasmonic Interferometric Imaging

Volume 13, Number 3, June 2021

Chang Wang

Xuqing Sun

Ruxue Wei

Xue Wang

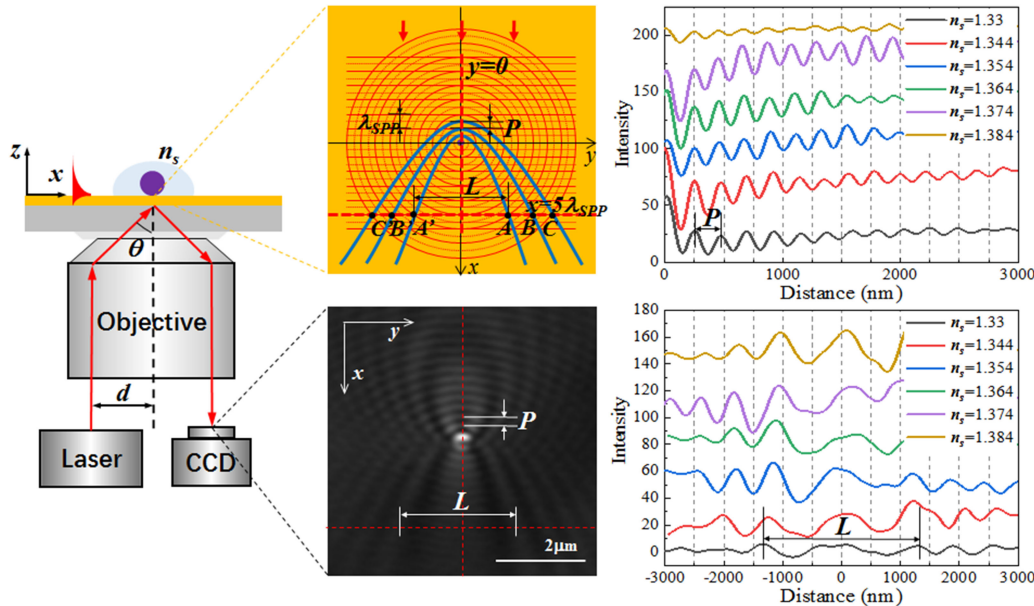
Hongyao Liu

Xiaojuan Sun

Fei Wang

Xinchao Lu

Chengjun Huang



DOI: 10.1109/JPHOT.2021.3072407

# Influence of Refractive Index to Plasmonic Interferometric Imaging

Chang Wang<sup>1,2</sup> Xuqing Sun,<sup>1,2</sup> Ruxue Wei,<sup>1,2</sup> Xue Wang,<sup>1,2</sup>  
Hongyao Liu,<sup>1</sup> Xiaojuan Sun,<sup>1,2</sup> Fei Wang,<sup>1,2</sup> Xinchao Lu<sup>1</sup>,  
and Chengjun Huang<sup>1,2</sup>

<sup>1</sup>Institute of Microelectronics of Chinese Academy of Sciences, Beijing 100029, China

<sup>2</sup>University of Chinese Academy of Sciences, Beijing 100049, China

DOI:10.1109/JPHOT.2021.3072407

This work is licensed under a Creative Commons Attribution 4.0 License. For more information, see  
<https://creativecommons.org/licenses/by/4.0/>

Manuscript received March 8, 2021; revised April 4, 2021; accepted April 6, 2021. Date of publication April 12, 2021; date of current version April 22, 2021. This work was supported in part by the National Key Research and Development Program of China under Grant 2017YFF0107002, in part by the Beijing Natural Science Foundation under Grant 4192063, and in part by the Scientific Research Equipment Project of Chinese Academy of Sciences under Grant YJKYYQ20190056. Corresponding authors: Xinchao Lu; Chengjun Huang (e-mail: luxinchao@ime.ac.cn; huangchengjun@ime.ac.cn).

**Abstract:** Plasmonic interferometric imaging has been widely used for fast and label-free detection to nano-objects, which associates the interference between launched and scattered surface plasmon polaritons (SPPs). As scattering of SPPs is affected by the characteristics of nano-objects, particle size, particle index and particle-interface distances have been retrieved from the imaging. Refractive index of dielectric, which tailors the resonant wavelength of launched SPPs, is also a key issue to plasmonic interferometric imaging. Yet, the influence of refractive index to plasmonic interferometric imaging has not been investigated. In this work, we connected the dielectric refractive index to the interferometric image intensity distribution, and found that both fringe periodicities and intensity profiles along SPP wavefronts were tailored by the refractive index, which is illustrated by using glucose solutions with different concentrations. Our research illustrates the pattern change of plasmonic interferometric imaging induced by dielectric refractive index, which not only paves the way for the basic understanding on the plasmonic interferometric imaging, but also provides a new potential visual method for real-time refractive index sensing and monitoring, which will be applied to food safety and environment monitoring.

**Index Terms:** Plasmonic, surface plasmon polaritons, interferometric imaging, refractive index.

## 1. Introduction

Surface plasmon polaritons (SPPs) are the collective oscillation of free electrons at metal-dielectric interface. Due to the capability of localizing the electromagnetic fields and dramatically enhancing the light-matter interactions in nanoscales, SPPs have been utilized in fast and label-free detection to nano-objects, i. e. single nanoparticles [1], viruses [2], DNAs [3], exosomes [4], and graphene sheets [5]. In order to reveal the physical mechanism of plasmonic interferometric imaging to single nanoparticles, the interaction between single nanoparticles and SPPs has been investigated extensively. The nanoparticles adsorb at the metal-dielectric interface, interact with the launched SPPs, and generate the localized field enhancement as well as scattering of SPPs. Finally, the plasmonic interferometric intensity distribution, which is induced by interference between the launching and scattering of SPPs, transforms to far field via leakage radiation [6] for fast imaging [1], [7], [8].

By now, lots of information can be retrieved from the plasmonic interferometric imaging. The wavevector, propagation length and propagation direction of launched SPPs have been obtained from the Fourier space interferometric imaging [9]. The size-dependent localized field enhancement of the silica and polystyrene particles has been used to determine the particle diameters [2], [10]. Moreover, the amplitudes and phases of scattered SPPs can be obtained from the plasmonic interferometric imaging based on a complex analysis algorithm for image reconstruction [11], and people acquired the diameter and refractive index of nanoparticles via retrieving the phase shift of SPP scattering from the image intensity distribution [12]. Also, through the plasmonic interferometric imaging, the transition from classical to quantum plasmonic couplings between a metal particle and metal surface is observed [13]. Refractive index of dielectric impacts the wavevector and propagation length of launched SPPs, which is also a key issue for plasmonic interferometric imaging. Yet, the influence of the refractive index to plasmonic interferometric imaging is still obscure.

In this work, we illustrated the influence of dielectric refractive index on plasmonic interferometric imaging induced by a single nanoparticle. By analyzing the interference between launching and scattering of SPPs, we found that both periodicities of interference fringes and intensity profiles along SPP wavefronts were tailored by resonant wavelength of launched SPPs, which is relevant to the dielectric refractive index. By retrieving fringe periodicities and intensity profiles along wavefronts, we demonstrated the intensity distribution change of plasmonic interferometric imaging dependent to refractive index of glucose solutions with different concentrations. This investigation provides a visual method to quickly observe the pattern change of interferometric imaging introduced by dielectric refractive index, which can be applied to the real-time analysis in the biomedication, food safety, and environment.

## 2. Simulation Results

Fig. 1(a) shows the physical mechanism of interference between launching and elastic scattering of SPPs. The propagation direction of launched SPPs is along  $x$  axis. Launched planar SPPs  $E_{SPP} = A_1 e^{i\beta x}$  interferes with scattered SPPs  $E_{Scat} = A_2 e^{i\beta \sqrt{x^2+y^2}}$ , where  $A_1$  and  $A_2$  are the amplitudes of  $E_{SPP}$  and  $E_{Scat}$ , respectively. The interferometric intensity distribution is expressed as:

$$I(x, y) = |E_{SPP} + E_{Scat}|^2 = |A_1|^2 + |A_2|^2 + 2A_1 A_2 \cos \varphi. \quad (1)$$

in which  $\varphi = \beta(\sqrt{x^2+y^2} - x)$  is the phase shift between  $E_{SPP}$  and  $E_{Scat}$ ,  $\beta = 2\pi/\lambda_{SPP}$ ,  $\lambda_{SPP}$  is the resonant wavelength of launched SPPs. As the maximum intensity emerges with  $\varphi = 0, 2\pi, \dots, 2m\pi$ , ( $m = 1, 2, 3, \dots$ ), the interference maxima are acquired from expression  $\sqrt{x^2+y^2} - x = m\lambda_{SPP}$ , which shapes the parabolic concentric fringes. With  $x < 0$ , the interference fringes are distributed periodically with periodicity  $P$  along the symmetric axis  $y = 0$ , the fringe periodicity  $P = \Delta x = \lambda_{SPP}/2$  can be obtained. With  $x > 0$ , the interference fringes show the opening of the parabolic fringes. We retrieved the plasmonic intensity profiles along wavefront of launched SPPs at the equiphase plane  $x = 5\lambda_{SPP}$  [12], [13], which is within the propagation length of SPPs at Au-air interface with excitation wavelength being 633 nm. At  $x = 5\lambda_{SPP}$ , we retrieved distances of the symmetric maxima counterparts A-A', B-B' and C-C' being  $2\sqrt{m^2 + 10m\lambda_{SPP}}$ . With  $m = 1$ ,  $L = 2\sqrt{11}\lambda_{SPP}$  is used to represent the distance between the symmetric maxima A and A', which is affected by the resonant wavelength of launched SPPs  $\lambda_{SPP}$ . The dispersion relation from Maxwell's equations connects the resonant wavelength of SPPs  $\lambda_{SPP}$  with refractive index of dielectric  $n_s$  [14]:

$$\lambda_{SPP} = \lambda_0 \sqrt{\frac{\varepsilon_m + n_s^2}{\varepsilon_m n_s^2}}. \quad (2)$$

where  $\lambda_0$  is the wavelength of incident light,  $\varepsilon_m$  is the real part of metal's complex permittivity. As a result, we derived the periodicity  $P = \frac{\lambda_0}{2} \sqrt{\frac{\varepsilon_m + n_s^2}{\varepsilon_m n_s^2}}$  and distance  $L = 2\sqrt{11}\lambda_0 \sqrt{\frac{\varepsilon_m + n_s^2}{\varepsilon_m n_s^2}}$  to manifest the influence of refractive index  $n_s$  to plasmonic interferometric imaging.

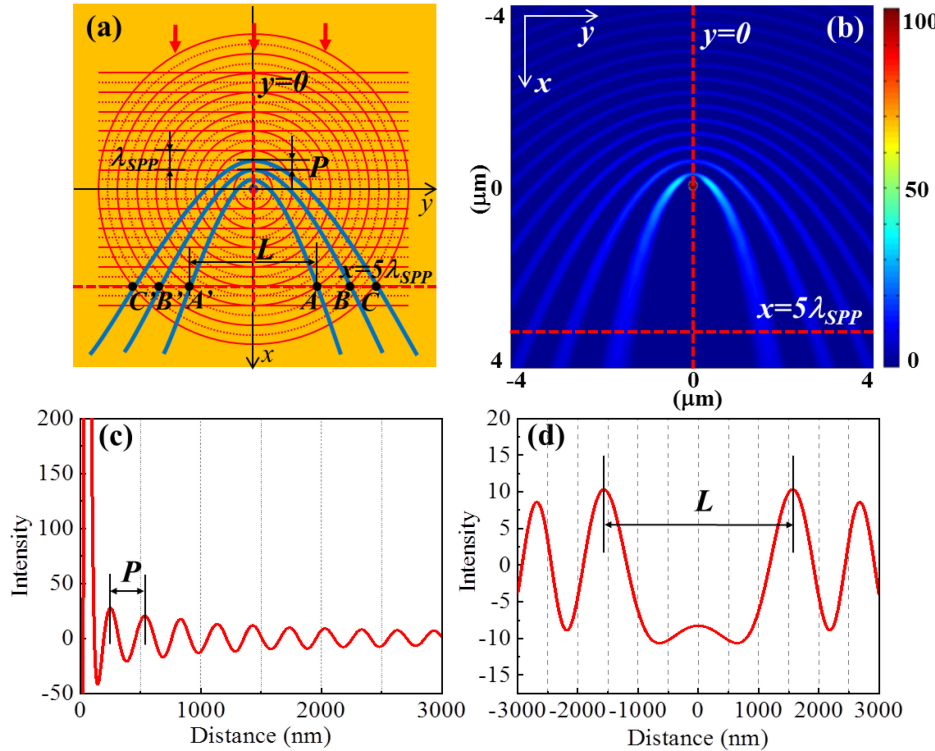


Fig. 1. (a) The diagram of the interference between launched and elastic scattered SPPs induced by a single nanoparticle,  $\lambda_{SPP}$  is the resonant wavelength of SPPs.  $P$  is the periodicity of interference fringes,  $L$  is the distance between symmetric interference maxima A and A'. The vertical red dash line manifests the symmetric axis  $y = 0$ , the horizontal red dash line manifests the wavefront of launched SPPs at  $x = 5\lambda_{SPP}$ , and A, A', B, B', C, C' indicate the interference maxima of plasmonic intensity profiles along the wavefront. The red arrows indicate the propagation direction of SPPs. (b) Simulated electric field intensity  $|E|^2$  at  $z = 5$  nm. The simulated intensity profiles along (c)  $y = 0$  and (d)  $x = 5\lambda_{SPP}$  (indicated by red dash lines in (b)) show the periodicity  $P$  and distance  $L$  between A-A'.

We simulated the electric field intensity  $|E|^2$  near the Au-air interface by using commercial finite difference time domain (FDTD) software from Lumerical Solutions, Inc. [15]. The total field scattered field (TFSF) plane wave is used as source with incident wavelength being 633 nm. The mesh of simulation is  $5 \text{ nm} \times 5 \text{ nm} \times 5 \text{ nm}$ , and the Au-air interface is set as  $z = 0 \text{ nm}$  plane. The single nanoparticle is positioned at the center of the interface  $(0, 0, 0)$ . The near-field monitor is set at  $z = 5 \text{ nm}$  apart from the interface. The permittivity parameters are set as  $\epsilon_{air} = 1$ , and  $\epsilon_{Au} = -10.8097 + 0.7896i$  [16]. The perfectly matched layer (PML) is set as the boundary conditions. The incidence angle  $\theta$  is set to be  $35.83^\circ$  for SPP launching at Au-air interface. Two simulations are conducted: the sample with nanospheres and reference without them. After subtracting the simulated reference from sample, the electric field intensity  $|E|^2$  of a single Au nanosphere with diameter of 200 nm at  $z = 5 \text{ nm}$  is shown in Fig. 1(b). After retrieving the contour along symmetric axis  $y = 0$  and SPP wavefront  $x = 5\lambda_{SPP}$ , the simulated intensity profiles were obtained, in which we get the periodicity  $P$  along symmetric axis and distance  $L$  between A-A', as shown in Figs. 1 (c) and (d). We also simulated the electric field intensity  $|E|^2$  near the Au-glucose interfaces with different concentrations, as shown in Fig. 2(a). We set the glucose concentrations ranging from 0 to 50% with increments of 10%. The corresponding refractive indexes of glucose  $n_s$  with different concentrations  $c$  are calculated as 1.33, 1.344, 1.354, 1.364, 1.374, and 1.384 by formula  $n_s = 0.001c + 1.334$  [17]. The incident angles are set to the excitation angles for SPP launching under different refractive index. Figs. 2 (b) and (c) show the fringe periodicities  $P$  and distances  $L$  retrieved from simulation. As  $n_s$  increase from 1.33 to 1.384,  $P$  change from 221.58 to

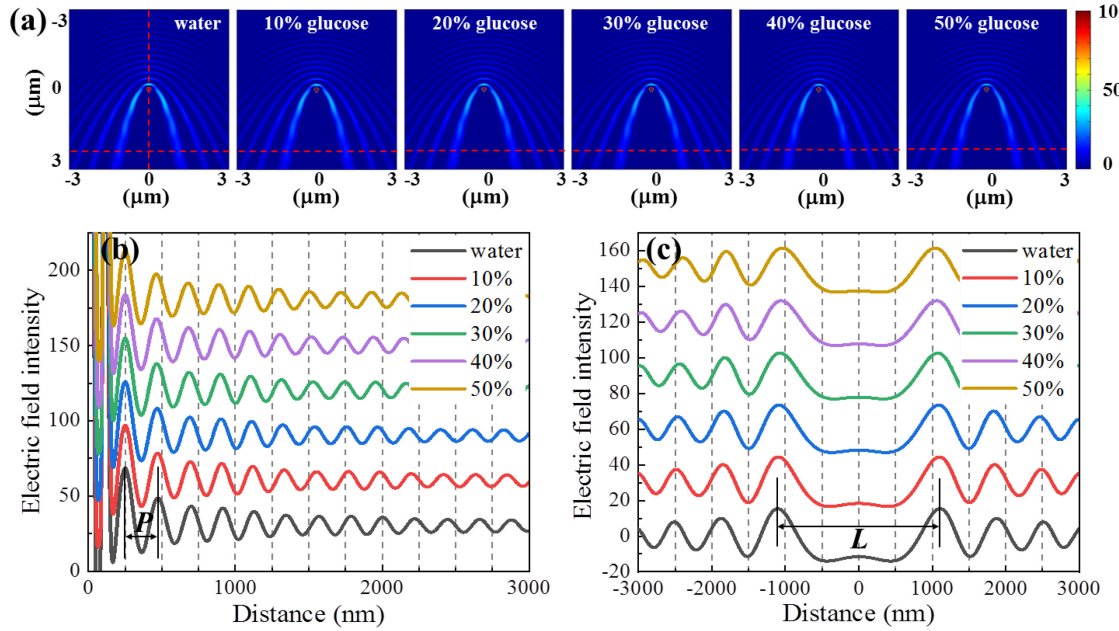


Fig. 2. (a) Simulated electric field intensity of a single 200 nm Au particle at Au-glucose interfaces with glucose concentrations changing from 0 to 50%. The vertical red dash line indicates  $y = 0$ , and horizontal red dash lines indicate  $x = 5\lambda_{SPP}$ . (b) The simulated electric field intensity profiles along  $y = 0$ . (c) The simulated electric field intensity profiles along  $x = 5\lambda_{SPP}$ . For clarification, the profiles with different concentrations are vertically shifted by 30.

212.27 nm and  $L$  decrease from 2208.85 to 2085.36 nm. As increasing glucose refractive index  $n_s$  induces decreased SPP resonant wavelength, both periodicities  $P$  and distances  $L$  show diminish.

### 3. Experiment and Discussion

The schematic of experimental setup is illustrated in Fig. 3(a). A 633 nm He-Ne laser is used to excite SPPs via objective coupled Kretschmann configuration. The numerical aperture (NA) of objective (Olympus APON100 $\times$ HOTIRF) is 1.7. A 50 nm Au film is evaporated on cover glass. The incident angle  $\theta$  for launching of SPPs is adjusted by a linear translation stage controlling the displacement  $d$  of the incident light. The 200 nm Au nanoparticles (Optical density is  $5 \text{ cm}^{-1}$ , Nanoseedz Ltd., Hongkong, China) are used to generate the plasmonic interferometric imaging. The Au nanoparticles solution is diluted to  $2.90 \times 10^{-3} \text{ mg/mL}$  with anhydrous alcohol and dispersed on Au film. The plasmonic interferometric images are obtained by a CCD camera (AVT Mako G319B, Allied Vision Technologies Inc). Twenty images of sample with SPP interference fringes, reflection background without fringes and CCD dark noise were captured respectively, and the average values were taken to reduce the experimental error. After subtracting the averaged reflection background and dark noise from the sample images with Image J software, we retrieved the periodicities of fringes  $P$  and distances  $L$  from the images. Fig. 3(b) shows the plasmonic interferometric imaging of a single 200 nm Au nanoparticle situating at Au-air interface with incident angle  $\theta = 36.5^\circ$ . After retrieving the contour along symmetric axis  $y = 0$  and SPP wavefront  $x = 5\lambda_{SPP}$ , we obtained the periodicity of fringes  $P$  and distance  $L$ , as shown in Figs. 3(c) and (d).

Experimentally, we used the glucose solutions with different concentrations to verify the intensity distribution change of plasmonic interferometric imaging dependent to refractive index  $n_s$ . At room temperature, glucose crystals are diluted by deionized water to solutions with concentrations  $c$  ranging from 0 to 50% and increments of 10%, whose corresponding refractive indexes  $n_s$  are 1.33, 1.344, 1.354, 1.364, 1.374, and 1.384, respectively [17]. The incident angles  $\theta$  are adjusted

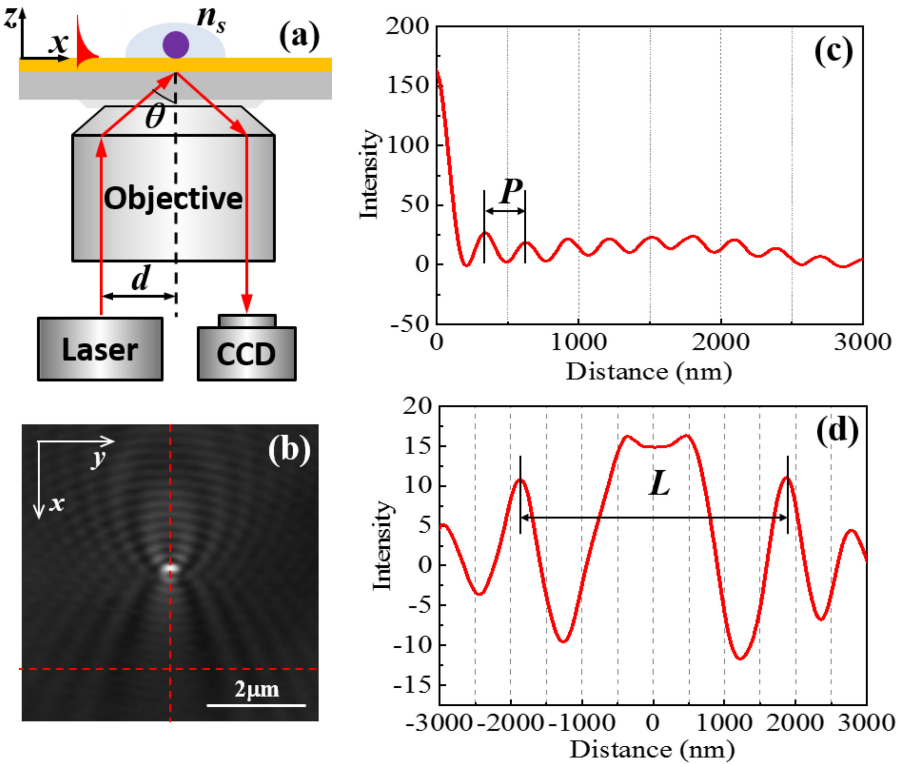


Fig. 3. (a) The schematic of plasmonic interferometric imaging setup. (b) The plasmonic interferometric imaging of a single 200 nm Au particle situating at Au-air interface. The plasmonic intensity profiles along (c)  $y = 0$  and (d)  $x = 5\lambda_{SPP}$  show the periodicity  $P$  and distance  $L$  between A-A'. The vertical red dash line manifests  $y = 0$ , and the horizontal red dash line manifests  $x = 5\lambda_{SPP}$ .

to obtain the SPP launching at Au-glucose interfaces with different concentrations. In Fig. 4(a), we obtained the plasmonic interferometric imaging of a single 200 nm Au particle situating at Au-glucose interfaces with different concentrations. The plasmonic intensity profiles along symmetric axis  $y = 0$  are shown in Fig. 4(b). We retrieved the periodicities of interference fringes by using Fourier transform to the profiles and taking the reciprocal of the frequency obtained from the spatial frequency domain. With the concentrations increasing from 0 to 50%, the periodicities  $P$  reduce from 223.52 to 210.32 nm. The plasmonic intensity profiles along  $x = 5\lambda_{SPP}$  are shown in Fig. 4(c) with distances  $L$  decreasing from 2573.19 to 2183.31 nm.

In Fig. 5, we compared the periodicities  $P$  and distances  $L$  extracted from the experimental and simulated results. Both experiment and simulation indicate decreasing  $P$  and  $L$  with increasing refractive index of glucose solutions  $n_s$ . Yet, by comparing the results, discrepancies between experiment and simulation exist, which is due to the defocusing of the imaging induced by the highly sensitive focal adjustment of high NA objective. As analyzed in Ref. [9], [11], [12], the influence of defocusing to the plasmonic interferometric imaging shows three characteristics with focal plane approaching the imaging plane. Firstly, more periodic fringes emerge with better contrast and the parabolic concentric fringes change to crossed shape. Secondly, the tailing experiences an intensity shift from dark to bright, which is due to the phase shift induced by imaging defocusing. Lastly, the opening angle of parabolic concentric fringes becomes larger which makes distances  $L$  increasing. In our study, the comparison between experiment and simulation shows agreement with all the three characteristics of defocused imaging. This is the reason that the distances  $L$  of our experimental results show large deviation with those of simulation.

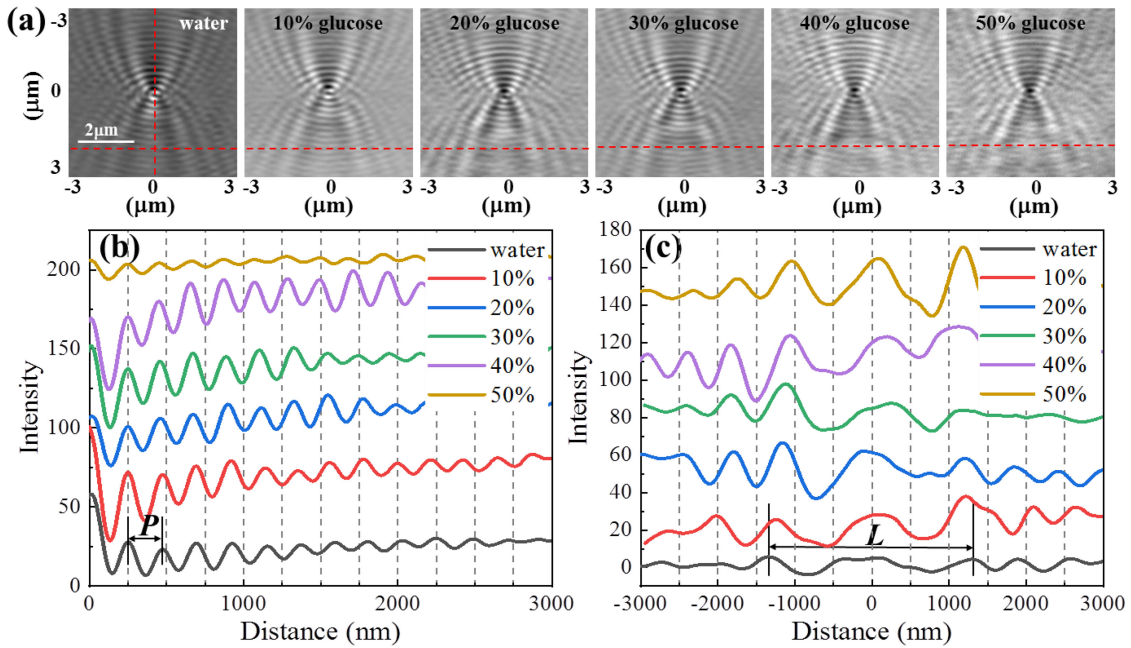


Fig. 4. (a) Plasmonic interferometric imaging of a 200 nm Au particle situating at Au-glucose interfaces with glucose concentrations changing from 0 to 50%. The vertical red dash line manifests  $y = 0$ , and the horizontal red dash lines manifest  $x = 5\lambda_{SPP}$ . (b) The plasmonic intensity profiles along  $y = 0$ . (c) The plasmonic intensity profiles along  $x = 5\lambda_{SPP}$ . For clarification, the profiles with different concentrations are vertically shifted by 30.

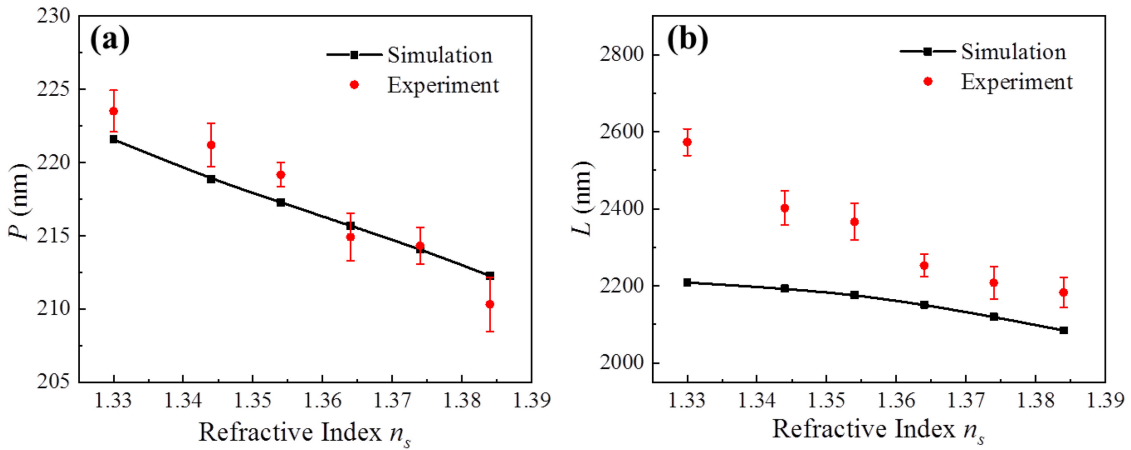


Fig. 5. The relationship of refractive index with (a)  $P$  and (b)  $L$  extracted from experimental and simulated results.

#### 4. Conclusion

In summary, we investigated the influence of dielectric refractive index to plasmonic interferometric imaging induced by a single nanoparticle. Based on the interference between launching and scattering of SPPs, we investigated that both the fringe periodicities  $P$  and distances  $L$  between interference maxima on SPP wavefronts were tailored by the refractive index. By retrieving the periodicities  $P$  and distances  $L$  from the plasmonic interferometric imaging with different refractive index  $n_s$ , we found that both of them decrease with increasing refractive index, which induced the

pattern change of plasmonic interferometric imaging. This study presents a method to real-time monitor the change of dielectric refractive index.

## Acknowledgment

We thank Prof. Weili Zhang from Oklahoma State University, Prof. Shaopeng Wang from Arizona State University, and Prof. Xianwei Liu from University of Science and Technology of China for their useful discussion.

---

## References

- [1] A. Zybin, Y. A. Kuritsyn, E. L. Gurevich, V. V. Temchura, K. Überla, and K. Niemax, "Real-time detection of single immobilized nanoparticles by surface plasmon resonance imaging," *Plasmonics*, vol. 5, pp. 31–35, 2010.
- [2] S. Wang *et al.*, "Label-free imaging, detection, and mass measurement of single viruses by surface plasmon resonance," *Proc. Nat. Acad. Sci.*, vol. 107, no. 37, pp. 16028–16032, 2010.
- [3] H. Yu, X. Shan, S. Wang, H. Chen, and N. Tao, "Plasmonic imaging and detection of single DNA molecules," *ACS Nano*, vol. 8, no. 4, pp. 3427–3433, 2014.
- [4] Y. Yang *et al.*, "Interferometric plasmonic imaging and detection of single exosomes," *Proc. Nat. Acad. Sci.*, vol. 115, no. 41, pp. 10275–10280, 2018.
- [5] R. Wei *et al.*, "Detecting the morphology of single graphene sheets by dual channel sampling plasmonic imaging," *Opt. Exp.*, vol. 28, no. 4, pp. 4686–4693, 2020.
- [6] A. Hohenau *et al.*, "Surface plasmon leakage radiation microscopy at the diffraction limit," *Opt. Exp.*, vol. 19, no. 25, pp. 25749–25762, 2011.
- [7] X. Sun *et al.*, "Imaging to single virus by using surface plasmon polariton scattering," in *Proc. SPIE Int. Conf. Optoelectron. Microelectronics Technol. Application*, Shanghai, China, 2017, vol. 10244, Art. no. 1024425.
- [8] E. Narimanov, "Resolution limit of label-free far-field microscopy," *Adv. Photon.*, vol. 1, no. 5, 2019, Art. no. 056003.
- [9] Y. Jiang, and W. Wang, "Point spread function of objective-based surface plasmon resonance microscopy," *Anal. Chem.*, vol. 90, no. 15, pp. 9650–9656, 2018.
- [10] X. Sun *et al.*, "Detecting a single nanoparticle by imaging the localized enhancement and interference of surface plasmon polaritons," *Opt. Lett.*, vol. 44, no. 23, pp. 5707–5710, 2019.
- [11] Y. Yang, C. Zhai, Q. Zeng, A. L. Khan, and H. Yu, "Quantitative amplitude and phase imaging with interferometric plasmonic microscopy," *ACS Nano*, vol. 13, no. 11, pp. 13595–13601, 2019.
- [12] C. Qian *et al.*, "Identification of nanoparticles via plasmonic scattering interferometry," *Angewandte Chemie Int. Ed.*, vol. 131, no. 13, pp. 4261–4264, 2019.
- [13] H. Wang, H. Yu, Y. Wang, X. Shan, H. Y. Chen, and N. Tao, "Phase imaging of transition from classical to quantum plasmonic couplings between a metal nanoparticle and a metal surface," *Proc. Nat. Acad. Sci.*, vol. 117, no. 30, pp. 17564–17570, 2020.
- [14] S. A. Maier, *Plasmonics Fundamentals and Applications*. New York, NY, USA: Springer, 2007.
- [15] Lumerical Solutions Inc., [Online]. Available: <http://lumerical.com/>
- [16] S. Babar, and J. H. Weaver, "Optical constants of Cu, Ag, and Au revisited," *Appl. Opt.*, vol. 54, no. 3, pp. 477–481, 2015.
- [17] Y. L. Fang, C. T. Wang, and C. C. Chiang, "A small U-shaped bending-induced interference optical fiber sensor for the measurement of glucose solutions," *Sensors*, vol. 16, no. 9, pp. 1460, 2016.